HHS Public Access

Author manuscript

Science. Author manuscript; available in PMC 2020 February 01.

Published in final edited form as:

Science. 2019 February 01; 363(6426): . doi:10.1126/science.aao0076.

Rhomboid distorts lipids to break the viscosity-imposed speed limit of membrane diffusion

Alex J.B. Kreutzberger[1,*], **Ming Ji**[1,*], **Jesse Aaron**[2], **Ljubica Mihaljević**[1], and **Siniša Urban**[*,#,1,2]

[1]Department of Molecular Biology & Genetics, Johns Hopkins University School of Medicine, Room 507 PCTB, 725 North Wolfe Street, Baltimore, MD 21205, USA

[2]Advanced Imaging Center, Janelia Research Campus, Howard Hughes Medical Institute, 19700 Helix Drive, Ashburn, VA 20147, USA

Abstract

Enzymes that cut proteins inside membranes regulate diverse cellular events including cell signaling, homeostasis, and host-pathogen interactions. Adaptations that enable catalysis in this exceptional environment are poorly understood. We visualized single-molecules of multiple rhomboid intramembrane proteases and unrelated proteins in living cells and planar lipid bilayers. Remarkably, only rhomboid proteins were able to diffuse above the Saffman-Delbrück viscosity limit of the membrane. Positioning/shape and hydrophobic mismatch induced by the rhomboid fold distorted surrounding lipids and propelled rhomboid diffusion. The rate of substrate processing in living cells scaled with rhomboid diffusivity. Thus, intramembrane proteolysis is naturally diffusion-limited, but cells mitigate this constraint by using the rhomboid fold to overcome the “speed-limit” of membrane diffusion.

One sentence summary:

With their catalysis limited by diffusion, rhomboid proteases evolved a way to break the ‘speed limit’ of diffusion in the membrane.

Enzymatic reactions enable all of life’s processes. While over a century of investigation has led to a sophisticated understanding of cellular enzyme catalysis, a different class of enzymes that harbour active sites inside the cell membrane was discovered more recently (1). Intramembrane proteases lie poised to discharge target proteins from the membrane in response to changing conditions, but the mechanism of these ancient and widespread enzymes remains poorly understood.

[#]correspondence: surban@jhmi.edu.

[*]joint first authors

Author contributions: SU conceived and designed the research, made all DNA constructs, performed all cell biology and some imaging experiments (Figs 1, 2, 5, and 6). JA performed some live-cell imaging and wrote all MatLab analysis code. AJBK performed all supported lipid bilayer experiments (Fig. 3), while MJ conducted all spin-labeling and EPR experiments (Fig. 4). LjM Halo-tagged RHBDL2 in the genome of HEK293T cells. SU wrote the manuscript and made the figures, and all authors approved the manuscript.

Competing interests: The authors declare no financial conflict of interest exists.

Data and materials availability: all data are available in the manuscript or the supplementary material.

Rhomboid proteases constitute the largest and best characterized superfamily of intramembrane proteases (2). They were discovered as initiators of epidermal growth factor (EGF) receptor signaling in *Drosophila*; insect rhomboid proteases cleave Spitz, liberating its EGF domain from the membrane to activate signaling in neighbouring cells (3). Although not yet fully understood, human rhomboid proteases have been implicated in wound healing and carcinogenesis (4), while a mitochondrial rhomboid plays roles in surveying mitochondrial health with implications for Parkinson's disease (5). Diverse protozoan parasites like malaria, trichomonas, and flesh-eating ameba that must initially adhere to host cells during pathogenesis use their rhomboid proteases ultimately to disassemble adhesive contacts with host cells (6, 7).

Evolution tuned enzymes to perform reactions with high efficiency, which is measured as the quotient of their catalytic rate (k_{cat}) and substrate-binding affinity (reflected in K_M). "Catalytically perfect" enzymes (efficiency quotients approaching 10^9 $M^{-1}s^{-1}$) are diffusion-limited; product formation is determined by how fast substrate/enzyme meet. In contrast, what features facilitate proteolysis within the membrane remain incompletely understood (8), but they must be quite different: kinetic investigations (9-12) revealed catalytic efficiency of intramembrane proteases ranges from 10^1-10^3 $M^{-1}s^{-1}$. This has led to the assumption that these proteases are far from being diffusion-limited enzymes.

The ability to investigate intramembrane proteases as pure proteins has greatly advanced our understanding of these enigmatic enzymes. However, in a living cell intramembrane proteases function in membranes that are crowded with ~50% protein (relative to lipid by weight), and encounter ~100-fold higher viscosity relative to aqueous enzymes (13). How do intramembrane proteases manoeuvre through the viscous and obstacle-filled membrane of a living cell? Here we visualized single molecules of 10 diverse rhomboid proteins and compared their behaviour to 7 unrelated membrane proteins, 3 substrates, and a phospholipid in living cells and planar supported lipid bilayers.

Rhomboid proteases diffuse unusually fast

To track single molecules of an intramembrane protease, we labeled rhomboid proteases in living cells with a series of bright and stable Janelia fluorophores (JF) that have been made compatible with self-labeling Halo tags (14). Treating HEK293T cells expressing low levels of Halo-RHBDL2 ('rhomboid-like-2') with Halo-tag-ligand (HTL)-JF646 facilitated detection of mobile point sources of fluorescence on the cell surface by single-molecule total internal reflection fluorescence (smTIRF) microscopy (Fig. 1A). Photobleaching kinetics were digital/quantized (15), which verified the spots to be single molecules, and gel electrophoresis revealed a single protein became labeled only in Halo-RHBDL2-expressing cells (Fig. 1B). Halo-RHBDL2 retained robust protease activity (Fig. 1C), and the fluorophore proved to be exquisitely stable. We could thus record movies, perform single-particle tracking, and fit the resulting tracks to model rhomboid's diffusive behaviour.

Membrane proteins displayed diffusion coefficients (D) typically ranging from ~0.0002-0.5 μm^2/sec when measured by single-particle tracking methods (16-26) (Fig. 1D and Table S1). Surprisingly, RHBDL2 diffusion exceeded that of the fastest multi-spanning membrane

protein previously recorded, namely the class A GPCR rhodopsin (25, 26). The rapid diffusion of rhodopsin is thought to underlie phototransduction (27). To determine whether there is a significant difference, we imaged both proteins under identical conditions using the fastest temporal resolution that we could achieve (64Hz, 15.7msec exposures). This revealed rhodopsin diffusion to be slightly faster (0.77±0.11 μm^2/sec) than previously measured, but RHBDL2 was faster still (0.81±0.08 μm^2/sec, Fig. 1E, $p=8.1\times10^{-12}$). Diffusion of endogenous RHBDL2 naturally expressed by HEK293T cells (that we Halo-tagged in the genome using CRISPR/Cas9) displayed the same properties (Fig. 1F). The seven transmembrane RHBDL2 diffused at a rate approaching its small, single-pass transmembrane substrate Ephrin B3 (Fig. 1G), although it should be noted that Ephrins cannot diffuse freely when they engage receptors during signaling.

We also evaluated any possible role of membrane organization or the underlying cytoskeleton on rhomboid mobility. Treating cells with microtubule destabilizing (nocodazole) or stabilizing (taxol) drugs, or actin depolymerizing (cytochalasin D, latrunculin B), severing (mycalolide B), or stabilizing (jasplakinolide) agents had little, if any, apparent effect on rhomboid diffusion (Fig. 1H). As such, rhomboid proteases diffuse rapidly and unaided in the plasma membrane of living cells.

We next evaluated whether unusually rapid mobility was a common feature of signaling rhomboid proteases by examining it in insects where rhomboid function was discovered and remains best-understood (3, 4). Assessing *Drosophila melanogaster* rhomboid-4 (DmRho4) mobility in *Drosophila* S2R+ cells (that also naturally express DmRho4) growing at 25°C revealed its diffusion was even faster (0.86±0.15 μm^2/sec) despite significantly lower temperature (Fig. 2A). DmRho4 harboring the Halo tag on the amino or carboxy terminus produced single JF646-labeled protein bands (Fig. 2B), and both were robustly active proteolytically (Fig. 2C). In this case, the seven transmembrane DmRho4 diffused much faster than its single-pass transmembrane substrate Spitz (Fig. 2D).

In order to evaluate whether the difference in diffusion between RHBDL2 and DmRho4 was due to differences in the proteins or the cells, we expressed DmRho4 in HEK293T cells and RHBDL2 in S2R+ cells. Interestingly, DmRho4 diffused significantly faster in HEK293T cells than RHBDL2, and RHBDL2 diffused slower than DmRho4 in S2R+ cells (Fig. 2E), indicating that rapid diffusion is largely a property of the specific rhomboid protein itself. However, both proteins diffused significantly faster in S2R+ cells at 25°C than in HEK293T cells at 37°C, highlighting the global influence of the host membrane on protein diffusion.

The rhomboid fold overcomes the viscosity limit of the membrane

The unusually rapid nature of rhomboid diffusion in living cells raised the possibility that its physical interaction with lipids might be different than experienced by other proteins. To evaluate this possibility we developed an in vitro planar lipid bilayer system to measure rhomboid diffusion directly in membranes of defined composition (Fig. 3A). Single-molecules of the *Escherichia coli* rhomboid GlpG, the most studied rhomboid protease, labeled either by linking a fluorophore to Halo (36 kDa) or directly to a single cysteine (0.1

kDa) resulted in remarkably similar diffusion (Fig. 3B). Mobility was thus entirely reliant on the viscosity experienced by the transmembrane core inside the membrane.

Remarkably, GlpG diffused very rapidly at 1.2±0.17 μm^2/sec (Fig. 3B) and much faster than any of the other membrane proteins that we analysed in parallel. In fact, plotting *D* versus radii of proteins with known structures revealed all 8 of our protein/lipid standards diffused according to the well established Saffman-Delbruck relation (Fig. 3C), which defines the physical viscosity limit of the membrane (28). In dramatic contrast, the only two rhomboid proteases of known structure diffused above the Saffman-Delbrück limit (Fig. 2C), and as fast or faster than the small, synthetic transmembrane peptide TatA-TM (0.9±0.13 μm^2/sec). As such, rhomboid proteins have the capacity to diffuse beyond the viscosity-imposed "speed limit" of the membrane.

What protein attribute could accelerate protein diffusion through a viscous, 2-dimensional fluid like the membrane? One characteristic but enigmatic structural feature of the rhomboid fold is its highly irregular shape that does not fit "neatly" into the membrane bilayer. Molecular dynamics simulations from a decade ago indicate that GlpG's protrusive shape and its hydrophobic belt, which is thinner than the hydrocarbon core of the surrounding membrane, distort annular lipids (29). Could this enable GlpG's rapid diffusion?

To test this hypothesis we compared protein diffusion in thinner membranes that more closely matched rhomboid's hydrophobic belt. Membrane proteins diffuse faster when the membrane bilayer is thinner (30), which we confirmed with all 8 of our protein/lipid standards (Fig. 3D). In contrast, thinning membranes to match rhomboid's hydrophobic belt uniquely slowed the diffusion of rhomboid proteins (Fig. 3D, E). Conversely, a natural lipid series that culminated in thicker membranes than is common at the plasma membrane accelerated diffusion even further, while the diffusion of membrane lipids followed no such trend (Fig. 3F). At the thickest membrane condition (Fig. 3F, PC 20:1), GlpG diffusion became indistinguishable from lipid diffusion (1.20±0.12 μm^2/sec versus 1.24±0.23 μm^2/sec, p=0.13). Thus, hydrophobic mismatch plays a major role in rhomboid's rapid diffusion.

Altered rhomboid position enhances lipid disruption and diffusion

Rhomboid proteins across evolution harbour cytosolic domains fused to their amino termini (2, 31). We wondered whether some of these appendages might further tune rhomboid diffusion by affecting its position in the membrane. Indeed, removing the cytosolic domain of GlpG resulted in slower, not faster, diffusion, despite the resulting truncated protein being ~30% smaller (Fig. 3G). Moreover, full-length, but not ΔN-GlpG, was able to diffuse more rapidly through a membrane near its transition "gelling" temperature, suggesting that its cytosolic appendage enhanced GlpG's ability to disrupt membrane lipid packing (Fig. 3H).

To examine experimentally whether full-length GlpG adopts a different position in the membrane relative to the well-studied ΔN-GlpG, we measured the depths of paramagnetic spin probes (32) on 11 positions encircling GlpG and ΔN-GlpG (Fig. 4A-B). Power saturation experiments revealed positions on the more rigid TM1/TM3/L1 loop region of GlpG experienced deeper membrane immersion, while positions on TM4/TM6 underneath

the active site on the opposite face of GlpG experienced more shallow positions in the membrane compared to ΔN-GlpG (Fig. 4C and Tables S2 and S3). Membrane immersion of TM5 and TM2 (between which substrate enters) was not altered by the presence of the cytosolic domain. As such, altered rhomboid positioning in the membrane induced by its cytosolic appendage further accelerates its diffusion through the membrane.

Rhomboid catalysis is diffusion-limited in living cells

While the exceptionally rapid diffusion of rhomboid proteases was intriguing, it remained unclear how it impacts rhomboid function in a cell. We therefore evaluated whether proteolytic rate in living cells relies on rhomboid diffusion.

Evaluating whether a step is rate-limiting requires accelerating it and assessing whether final product formation is correspondingly elevated. Increasing diffusion selectively is challenging because most treatments do so by altering temperature or protein concentrations, but these changes also have strong effects on catalysis. We thus sought a pharmacological agent that might alter phospholipid packing and thus increase overall diffusion. We ultimately found that ionomycin precomplexed with magnesium dramatically lowered the transition temperature of phospholipids in vitro (Fig. 5A), and accelerated the mobility of all plasma membrane proteins that we examined ~2-fold (Fig. 5B-C).

Remarkably, increasing diffusion in living cells elevated processing of Ephrin B3 by RHBDL2 ~3 fold (Fig. 5D). Both increased diffusion and proteolysis occurred with ionomycin precomplexed with only magnesium (in the absence of calcium), and neither increased when calcium was released from intracellular stores via thapsigargin (Fig. 5C and D). Thus, stimulating diffusion/proteolysis was not dependent on triggering calcium signaling, but instead resulted generally from ferrying divalent metal ions across the plasma membrane (consistent with calorimetry analysis, Fig. 5A). In addition to the natural substrate Ephrin B3, proteolysis of a different substrate, but not a non-substrate, was also stimulated by magnesium-complexed ionomycin but not thapsigargin (Fig. 5E). The stimulation occurred in the presence of both cycloheximide (Fig. 5F) and brefeldin A (Fog. 5G), indicating it was independent of protein synthesis or trafficking. The ultimate rate of RHBDL2 proteolysis in living cells thus depends on diffusion.

Since magnesium-complexed ionomycin increased the diffusion of all membrane proteins tested, we also examined the effect of selectively slowing rhomboid diffusion alone. We tethered RHBDL2's extracellular Halo tag to large quantum dots (22.5 nm diameter) through a flexible linker. This treatment decreased RHBDL2-HaloC diffusion by ~20-fold (Fig. 6A), and correspondingly halved the rate of substrate proteolysis (Fig. 6B), presumably because substrates remained free to diffuse. The same high concentration of quantum dots had no effect on the activity of NHalo-RHBDL2 (because NHalo is cytosolic).

Finally, while we deliberately focused on rhomboid proteases involved in signaling, we concluded our studies by examining whether rapid diffusion is a property common to the rhomboid family fold (including inactive rhomboid proteins that serve chaperoning functions). All rhomboid proteins diffused very rapidly, but the *Entamoabe histolytica* and

Trichomonas vaginalis rhomboid enzymes proved to be the fastest rhomboid proteins encountered (Fig. 6C), exhibiting the highest D (0.97 μm^2/sec) we measured for any multi-spanning membrane protein in cells using single-particle tracking. Interestingly, both of these parasites are non-invasive and use their rhomboid enzymes to untether themselves from host cells (7, 33). Under these conditions, the adhesive zones would be stationary, and as such proteolysis would rely entirely on rhomboid diffusion for efficient substrate processing. Rapid protein diffusion is thus a widespread feature of the rhomboid fold across evolution that might be fine-tuned to meet the specific needs of the organism in which rhomboid functions.

Concluding perspectives and implications

Although serine protease catalysis originated by convergent evolution on at least a dozen separate occasions (34), only serine protease catalysis inside the membrane faces the challenge of hindered diffusion. This unique context provided us with an opportunity to determine that a protein can actually overcome the viscosity limit of the membrane.

The mechanism underlying this unusual activity is multifaceted: the rhomboid fold adopts a protrusive and highly irregular shape within the membrane, and introduces hydrophobic mismatch with surrounding lipids, the combination of which apparently synergize to act as an “ice-breaker” that distorts lipid interactions and facilitates rhomboid mobility (Fig. 7). In fact, Molecular Dynamics simulations suggest lipid distortion is severe near the protrusive L1 loop that we found gains deeper membrane insertion when the cytosolic domain is present. The altered position of the transmembrane core thus probably leads to an even more frustrated, lipid distorting position that enhances diffusion. These features may explain why rhomboid members that lost protease activity nevertheless play a variety of important roles (35). Accordingly, we propose that the defining and evolutionarily selected feature of the rhomboid fold is local membrane distortion rather than transmembrane helix binding, which has been the most likely explanation until now (35).

What might this, in turn, reveal about rhomboid’s functions in a cell? Intramembrane proteases are unlike other membrane proteins involved in signaling, because each protein-protein encounter generates only a single molecule of signal. Other signaling membrane proteins seldom face this challenge: even transmembrane receptors that need to encounter partners in the membrane form stable signaling complexes once dimers/oligomers assemble, and then signal persistently. Reiteratively seeking out substrates in the membrane is thus an uncommon demand faced by rhomboid proteases, which is exacerbated when they must process immobilized substrates like parasite adhesion molecules or receptor-engaged ligands like B-type Ephrins. Analogous functions could have provided the evolutionary pressure that sculpted the rhomboid fold into a diffusion-accelerating module.

Hydrophobic mismatch and local membrane deformation has been documented in a variety of unrelated proteins and is thought to modulate their function in different ways (36). The large number of proteins that are packed into the membrane implies other membrane enzymes likely faced similar diffusive challenges and may have evolved similar diffusion-enhancing strategies.

MATERIALS AND METHODS

Animal Cell Culture

Human HEK293T cells (CRL-11268, purchased from American Type Culture Collection) were grown in DMEM (Life Technologies) supplemented with 2mM L-glutamine, 10mM Hepes pH 7, 10% fetal bovine serum (F4135, Sigma), and 10 μg/ml gentamicin at 37°C and humidified 5% CO_2. *Drosophila melanogaster* S2R+ cells (stock #150, purchased from the *Drosophila* Genomics Resource Center) were grown in Schneider's *Drosophila* medium (Life Technologies) supplemented with 10% fetal bovine serum and 10 μg/ml gentamicin at 25°C in sealed T75 flasks.

Endogenous RHBDL2 was tagged with Halo in HEK293T cells using a CRISPR-Cas9 strategy (37, 38). 36 nucleotide long homology arms were introduced onto both ends of the Halo repair template by PCR with primers (F: 5'-TGT CCT TCT GGG GAG GAG GGA GGA CCA AGG ACA ATG GCA GAA ATC GGT ACT GGC-3' and R: 5'-ATT CAT GCT CTC CAT CTC CAG ATC ATG AAC AGC AGC GTT ATC GCT CTG AAA GTA CAG ATC CTC -3'). The guide RNA (5'-ATGAACAGCAGCCATTGTCC-3') was cloned into the PX459 vector, and the repair template and guide RNA were then delivered together (in a 30:1 pmol ratio) by transfection with X-tremeGENE HP. Positively transfected cells were selected 48h after transfection with 2μg/ml puromycin, and selection was continued until all the cells in the negative control died (96h). The Halo insertion was verified by DNA sequencing.

Rhomboid Labeling in Live Cells

HEK293T and S2R+ cells were seeded in 35 mm dishes onto coverslips (CS-25R15, Warner Instruments) that had been freshly washed in 1M KOH for 30 minutes in a sonic cleaner (8510, Branson), thoroughly rinsed in Milli-Q water, and sterilized by UV irradiation. For some early experiments, coverslips contained fiduciary dynabead-streptavidin magnetic beads that were attached to poly-L-lysine-coated coverslips via NHS-biotin treatment (but the stability of the microscope obviated their use). ~24 hours after seeding onto coverslips, HEK293T cells were transfected with 5 μl X-tremeGENE HP (Roche) and 1 μg of total plasmid DNA, but to ensure low levels of expression, only 1/1,000th of the total DNA (1 ng of 1 μg) encoded RHBDL2, EhROM1, TvROM1, RHBDL3/Ventrhoid, iRhom1, iRhom2, or Rhodopsin in pHTN and/or pHTC (Promega) while the remainder was pBluescript. To track substrates, the self-labeling SNAP tag was cloned from pSNAPf (New England Biolabs) and used to replace GFP in pcDNA3.1-GFP-Ephrin B3-Flag or pRmHaA3-GFP-Spitz. S2R+ cells were similarly transfected as detailed previously (31), but 48 hours after seeding onto coverslips, and with pRmHa3-DmRho4 constructs into which the Halo tag was cloned. Protein expression was induced with 0.5 mM $CuSO_4$ 24 hours after transfection.

18 to 24 hours after seeding HEK293T cells harbouring endogenously tagged RHBDL2, or transfection of HEK293T cells, or inducing protein expression in S2R+ cells, coverslips were incubated with 20 nM Halo-tag ligand (HTL)-JF549, 1 nM HTL-JF646, and/or 0.5-250 nM SNAP-tag ligand (STL)-JF549 for 20 minutes in complete medium at 37°C and 5% CO_2 (25°C for S2R+cells). HEK293T cells were washed three times with FluoroBrite DMEM

freshly supplemented with 2mM L-glutamine, 10% fetal bovine serum, and 10 μg/ml gentamicin and imaged at 37°C, or for protein analysis lysed directly in reducing Laemmli SDS sample buffer and boiled for 10 min prior to gel electrophoresis. S2R+ cells were similarly labeled except in Schneider's *Drosophila* medium (Life Technologies) supplemented with 10% fetal bovine serum and 10 μg/ml gentamicin, and imaged at ~25°C.

For rapid imaging at the 64 Hz frame rate (15.7 msec exposures), cells were "instantly labelled" by incubating with HTL-JF646 for 20 min, and, following a single rinse, imaged immediately. Background was undetectable because JF646 is chromogenic and thus not fluorescent until bound to the HaloTag. This rapid labeling protocol facilitated capturing molecules on the cell surface before some were endocytosed.

Protein Analysis

Whole-cell protein lysates in reducing Laemmli buffer from HTL-JF646-labeled HEK293T or S2R+ cells were resolved by electrophoresis through 4-20% tris-glycine SDS polyacrylamide gels or 4-12% Bolt SDS polyacrylamide gels (Invitrogen) at 120-140V, and imaged on an Odyssey infrared scanner (LiCor Biosciences) in the 700 nm channel to visualize JF646-labeled proteins.

Single-Molecule Live-Cell TIRF Microscopy

HEK293T and S2R+ cells were imaged immediately following labeling/washing using a custom single-molecule TIRF microscope that was built on an Olympus base. Coverslips were mounted in 25 mm cell culture chambers (SKE Research Instruments) and imaged on a Piezo stage through a heated, oil-immersion Olympus 1.49 NA 60x objective. JF549 and JF646 were excited by 532 nm and 640 nm lasers (Obis and Verdi, Coherent), respectively, and emitted photons in each channel were detected separately with two electron-multiplying charge-coupled device (EMCCD) cameras (iXon, Andor). Exposure times and frame rates used were either 15.7 msec (64 Hz) or 40 msec (25 Hz). Typically movies were collected for 2,000 continuous frames. When fiduciary beads were used to stabilize possible stage drift during imaging, beads were tracked using a separate infrared camera, and the stage x/y/z position was automatically adjusted every second (1 Hz) (39).

For magnesium-ionomycin treatment experiments, several cells were imaged in complete Ca-free DMEM media as described and the last cell was used to document the 'pre-addition' condition. Then media containing the desired drug was added directly to the imaging chamber to achieve final concentrations of 6 μM ionomycin (I9657, Sigma) and 2 mM $MgCl_2$. After a 5 min equilibration, the same cell was imaged ('post-addition') before moving onto imaging additional cells. For cytoskeletal stabilizing/destabilizing treatments, cells were incubated in the presence of the drug as indicated below, and then mounted and imaged in fresh media containing the drug. Specific conditions used before and during imaging were: 20 μM cytochalasin D (C2618, Sigma) for 45 minutes to 6 hours, 10 μg/ml latrunculin A (L5163, Sigma) for 2.5 hours, 10 μM mycalolide B (sc358736, ChemCruz) for 3.5 hours, 10 μM jasplakinolide (J7473, Life Technologies) for 4 hours, 10 μM paclitaxel/taxol (P3456, Molecular Probes) for 2.5 hours, and 33 μM nocodazole (M1404, Sigma) for 1 to 2 hours.

Single-Particle Tracking and Diffusion Model Fitting

smTIRF movies were imported into Fiji software, and single particle tracking was performed with Mosaic, which has been evaluated to produce reliable tracking results (40, 41). All movies were manually evaluated for quality, and single cells were cropped for individual tracking. To improve particle detection, background was subtracted with a rolling ball radius of 5 pixels and a mild Gaussian filter was applied with a sigma radius = 0.6. Mosaic tracking parameters used were a particle radius of 3.0, per/abs of 1.5-5.0, cut-off of 20, link of 1 (thus not allowing any frames to be skipped), and displacement of 1.5 to 4.5 pixels. The quality of the tracking (particle recognition in individual frames, and particle linkage across frames) was manually inspected to ensure that most particles were detected, and links between different nearby particles ('jumps') were absent or very rare.

The resulting tracks from individual cells were imported into MatLab (MathWorks) running on a Linux platform, and diffusion was modeled with custom-written code according to the equation: $r^2 = 4Dt^{\alpha}$. Pixel size was 177 nm, the minimal allowed continuous track length was set to 10, the minimal accepted R^2 threshold of the fits was set to 0.7 for *D*/alpha <5, which further served to remove any artifactual tracks. For any given condition, hundreds to thousands of tracks per cell were analysed from at least 5 separate cells individually and averaged, and in most cases tracks from 10 or more individual cells were used to compute the diffusion coefficient. Track lengths ranged from 10 to 1,733 steps, and no correlation was observed between track length and diffusion coefficient (Pearson's correlation coefficients ranged from −0.15 to −0.20).

Statistical Analyses

Diffusion parameters and protease activity were evaluated for statistical significance using an unpaired two-sided student's t-test with unequal variance in MatLab and Prism, respectively. Effect size of statistically significant differences were evaluated using the Cohen statistical method to compute d-values.

In Vivo Rhomboid Proteolysis Assay

To assess rhomboid protease activity, HEK293T cells were seeded into treated or CellBIND 6-well plates (Costar), and transfected according to manufacturer's instruction with 5 µl X-tremeGENE-HP (Roche) and 1 µg of total plasmid DNA when they reached ~75% confluence. To ensure low protein levels, only 1 ng of HA-tagged RHBDL2 in pcDNA3.1, and 2.5 ng of GFP-EphrinB3-Flag or SNAP-EphrinB3-Flag in pcDNA3.1 were used, with the remaining DNA being pBluescript. 18-28 hours post-transfection, media was removed from cells and fresh serum-free media containing 10 µM Batimastat was conditioned for an addition 24 hours. For ionophore treatment, cells were washed with Ca-free DMEM 18-28 hours post-transfection and incubated in 1 mL of Ca-free DMEM supplemented with 2mM L-glutamine, 10mM Hepes pH 7, 10 µg/ml gentamicin, 15 µM free-base ionomycin (I9657, Sigma) and 8 mM $MgCl_2$ (or 15 µM thapsigargin, T9033, Sigma) at 37°C in an incubated digital heat block (VWR) for the indicated times before media was removed and cells lysed in reducing Laemmli SDS sample buffer and boiled for 10 minutes. S2R+ cells were co-transfected with X-tremeGENE-HP and a GFP-tagged Spitz substrate in pRmHa3 exactly as described previously (31). Proteins were resolved on 4-20% tris-glycine SDS

polyacrylamide gels (Invitrogen), electro-transferred onto nitrocellulose using the semi-dry method (Trans-Blot Turbo, BioRad), probed with rabbit anti-GFP (ab32146, AbCam), rat anti-HA (3F10, Roche) and/or anti-Flag (F7425, Sigma) affinity-purified antibodies, visualized with anti-rat-IRDye680lt and/or anti-rabbit-IRDye800cw, and quantified on an Odyssey infrared scanner using ImageStudio software (LiCor Biosciences). Untransfected cells were routinely analysed in parallel to confirm antibody specificity.

Quantum Dot Conjugation and Analysis

Qdot 705 ITK amino PEG quantum dots (021561MP, Molecular Probes) were reacted with a 40-fold molar excess of HaloTag succinimidyl (O4) ester ligand (P675A, Promega) in 50 mM borate pH 8.3 buffer for 1 hour at room temperature. Unreacted ester was quenched with 50 mM Tris for 15 minutes, removed using size exclusion chromatography, and HTL-PEG-Qdot705 quantum dots were tethered to cell surface RHBDL2-Halo by adding HTL-PEG-Qdot705 to transfected cells growing in complete media. After incubating at 37°C for 1 hour, cells were washed into serum-free media (supplemented with L-glutamine, 20 μM Batimastat, and Brefeldin A), and substrate proteolysis was examined after 1, 2, and 3 hours by lysing cells in reducing Laemmli SDS sample buffer, boiling for 10 minutes, and quantification by western analysis as described above.

Differential Scanning Calorimetry

Small unilamellar vesicles were prepared from dimyristol-phosphatidylcholine (850345C, Avanti Polar Lipids) as described previously (9), and analyzed at a concentration of 3 mM phospholipid in buffer containing 50 mM HEPES pH 7.3, 150 mM NaCl 10 mM $MgCl_2$. Samples were repeatedly scanned at a rate of 10°C/hr from 4°C to 40°C in a capillary VP-DSC (GE Healthcare) operating in high-sensitivity mode.

Halo-Tagged Protein Expression and Purification

Bacterial open reading frames (ORFs) of LacY, MsbA, GlpF, AqpZ, AarA and GlpG were cloned into a pET21 vector harboring a C-terminal Halo-His tag, C20S and E43A were introduced into AqpZ and GlpF, respectively, for analysis of their monomeric states, and the entire ORFs were sequenced as described recently (15). The resulting expression plasmids were transformed into BL21(DE3) cells, and grown in 2L of LB media containing 100 μg/mL ampicillin as a selection marker at 37°C and with shaking at 250 rpm. Protein expression was induced with 100 μM IPTG at an OD_{600} between 0.6 and 0.7, and the cultures were subsequently grown overnight at 16°C. Cells were pelleted at 6,000 rpm in an Avanti JA26 XPI high-speed centrifuge (Beckman), resuspended in PBS containing a protease inhibitor cocktail (Roche), and lysed in a M-110A microfluidizer (Microfluidics) operating at 17,500 psi. Membranes were pelleted by ultracentrifugation at 60,000rpm in a 70Ti rotor (Beckman), resuspended in PBS, and solubilized overnight by adding 2% DDM. Membrane debris was removed by ultracentrifugation at 60,000 rpm for 30 minutes in a 70Ti rotor and the supernatant was incubated with cOmplete His-tag resin (Roche) for ~2 hours at 4°C. Resin was washed, and proteins were eluted with 500 mM imidazole. Protein purity was verified by SDS-PAGE, visualized using BandIt protein stain, and fluorescence scanned with a 700nm laser of an Odyssey infrared imager (LiCor Biosciences)

Planar Supported Lipid Bilayer Formation

Planar bilayers reconstituted with the desired protein were formed employing a three-step method (42). First, 35 mm round No 1.5 glass coverslips (Warner Instruments) were cleaned by dipping in 3:1 sulfuric acid:H_2O_2 for 10 minutes and then thoroughly rinsed using purified water. The first leaflet of the bilayer was deposited using Langmuir-Blodgett transfer. A lipid monolayer of the desired composition was prepared on a pure water surface of a KSV NIMA Langmuir-Blodgett trough (Biolin Scientific) by adding drops of desired lipid composition in a chloroform solution. The solvent was allowed to evaporate for ~10 minutes and the monolayer was compressed to reach a surface pressure of 32 mN/m. Slides were submerged rapidly (200 mm/min) into the trough and slowly withdrawn (5 mm/min) while maintaining a constant surface pressure.

Proteoliposomes containing the desired reconstituted Halo-tagged protein were made as described previously (43) with minor modifications. Briefly, chloroform was first evaporated from desired phospholipids (Avanti Polar Lipids) in a pear-shaped flask using a rotary evaporator, and then dried under high vacuum overnight. Liposomes were formed by resuspending dried lipid films in desired buffer, subjecting them to 5 freeze thaw cycles using dry ice and a water bath, and then passing 15 times through a 100 nm NanoSizer extruder (T&T Scientific). Liposomes were then incubated with protein to achieve the desired lipid-to-protein ratio of 10^6:1. After 15 minutes of incubation, proteoliposomes were rapidly diluted to a volume of 10 mL, incubated for another 10 minutes, and then pelleted at 50,000 rpm for 30 minutes in a MLA-55 ultracentrifuge rotor (Beckman). The pellet was resuspended in 50 mM Tris pH 7.4, 150 mM NaCl.

Proteoliposomes were then incubated at room temperature for 1 hour at a nominal concentration of 100 μM lipid to deposit the second leaflet and thus completing the planar bilayer of the desired lipid and protein composition. Finally, Halo-tagged proteins were labeled by incubating with 1 nM HTL-JF646 for 10 minutes, and excess label and proteoliposomes were removed by washing coverslips with buffer.

smTIRF Imaging and Analysis of Planar Supported Bilayers

Planar supported lipid bilayers were imaged using a Nikon Eclipse Ti-E TIRF microscope with a 100x/1.49 Apo TIRF oil objective and excited with a 640 nm laser. Each planar bilayer was imaged in 5 randomly selected areas for 1 minute using 30 msec exposure times. Single particle tracking was performed as described for live cells, except that a displacement of 6 pixels was allowed. Tracking was manually inspected to ensure data quality. Diffusion was modeled as described for live cells, except using a pixel size of 107 nm and R^2 threshold of 0.5. Five movies were analyzed for each bilayer condition and the results were pooled.

Protein Expression and Purification for EPR Spectroscopy

Engineered variants of *E.coli* GlpG lacking its endogenous cysteine (C104V) and containing a single cysteine at each desired position were over-expressed as N-terminal His-tagged fusions in *E. coli* C43(DE3) cells. Cultures were grown in LB media with 100 μg/mL ampicillin at 37 °C in a LEX-48 Parallel Bioreactor System (Harbinger Biotech). When the

absorbance at 600 nm of the culture reached 0.8 (ΔN-GlpG), or 0.7 (full-length GlpG), the reactions were induced by adding 300 μM IPTG for 17-19 h at 30 °C (ΔN-GlpG), or 23 °C (full-length GlpG). Bacterial cell lysates were prepared using a microfluidizer operating at 17,500 psi and cell membranes were pelleted by ultracentrifugation at 350,000*g* for 30 min. GlpG protein was solubilized from membranes in 2% nonyl-β-D-glucopyranoside (NG) (ΔN-GlpG), or dodecyl-β-D-maltoside (DDM) (full-length GlpG) overnight at 4 °C, followed by ultacentrifugation at 350,000g for 30 min to remove insoluble contents. His-GlpG was affinity-purified with His-tag resin (Roche) and eluted using 300 mM imidazole. Purity of enzymes was determined by Nu-PAGE stained with blue and quantified on an Odyssey Imager (LI-COR Biosciences). Imidazole in the purified protein sample was removed by using PD-10 desalting columns (GE Healthcare).

Site-Specific Nitroxide Labeling

A 4 μL 100 mM 1-Oxyl-2,2,5,5-tetramethylpyrroline-3-methyl)methanethiosulfonate (MTSL, Toronto Research Chemicals, Canada) stock was diluted into a 500 μL DMSO and was then added to a 3.5 ml ~5 μM GlpG sample in 25 mM Tris, pH 7.4, 300 mM NaCl, 10% glycerol, 0.4% NG (ΔN-GlpG), or 0.1% DDM (full-length GlpG), with a final molar MTSL:GlpG ratio of ~20:1. The reaction vessel was covered with aluminum foil and incubated at room temperature for ~4 hrs, and then excess free spin label was first removed by running the sample through a PD-10 column (GE Healthcare). The N-terminal His_6 tag was removed by thrombin cleavage at 4 °C overnight, and the labeled samples were further purified by using a Superdex-200 column (GE Healthcare) in a buffer containing 25 mM Tris, 300 mM NaCl, 10% glycerol, 0.4% NG (ΔN-GlpG), or 0.1% DDM (full-length GlpG).

Spin-Labeled GlpG Reconstitution

A total of 600 μg of 1-palmitoyl-2-oleoyl-*sn*-glycero-3-phosphocholine (POPC) or *E. coli* liposomes were mixed with 300-600 pmol of labeled GlpG protein. This coreconstitution mix was rapidly diluted ~20-fold with 10 mM HEPEs (pH 7.0), 10 mM NaCl to promote reconstitution by reduce the detergent concentration below its critical micelle concentration. Proteoliposomes were collected by ultracentrifugation at 600,000g for 1 h using an Optima MAX-XP ultracentrifuge (Beckman). The pellet after ultracentrifugation was resuspended in 25 mM Tris (pH 7.4), 150 mM NaCl.

CW-EPR Spectroscopy

X-band continuous-wave electron paramagnetic resonance (CW-EPR) experiments were performed in a EMXmicro spectrometer equipped with a PremiumX ultra low noise microwave bridge and a high-sensitivity ER4119HS resonator (Bruker Biospin, Billerica, MA) at four different temperatures (310°K, 298°K, 288°K, and 278°K) using an ER4141VT temperature control unit (Bruker Biospin, Billerica, MA). ~25 μL of spin-labeled GlpG that had been reconstituted into *E.coli* liposomes was loaded into a quartz capillary tube that was sealed with wax. The modulation frequency, amplitude and sweep width in the experiments were set at 100 KHz, 2 G and 150 G, respectively. The CW-EPR spectra were fit by the microscopic order macroscopic disorder (MOMD) model using the NLSL program as described in (44).

CW-EPR Power Saturation Experiments

Continuous-wave power saturation experiments were performed in an ER4123D resonator (Bruker Biospin, Billerica, MA) at room temperature. Spin-labeled proteins were reconstituted into liposomes comprised of POPC, and ~5 μL was placed into a gas-permeable TPX capillary tube (Molecular Specialties, Inc.). Power saturation curves for different GlpG samples were measured between 0.5 mW to 63 mW under three different conditions: (1) equilibration under atmospheric oxygen (20%); (2) equilibration under N_2; (3) equilibration under N_2 with 30 to 100 mM NiEDDA. Accessibility parameters were calculated as following (45):

$$\Pi(X) = \left[\frac{P_{1/2}(X)}{\Delta H_{pp}(X)}\right] - \left[\frac{P_{1/2}(N_2)}{\Delta H_{pp}(N_2)}\right] \quad (1)$$

where X represents either O_2 or NiEDDA, Π represents the accessibility parameter for O_2 or NiEDDA, $P_{1/2}$ is the power at which half-saturation occurs and ΔH_{pp} is the average peak to peak line width within the linear region of the power saturation curve. These two values were obtained directly from experimental data using Xenon software (Bruker Biospin, Billerica, MA). The immersion depth parameters were calculated based on the following equation:

$$\Phi = \ln\left[\frac{\Pi(O_2)}{\Pi(NiEDDA)}\right] \quad (2)$$

where Φ is the immersion depth parameter. The immersion depth of the R1 chains of MTSL were calculated as described in (46):

$$\text{depth}\,(\text{Å}) = 4.81\Phi + 4.9 \quad (3)$$

Supplementary Material

Refer to Web version on PubMed Central for supplementary material.

Acknowledgements

We are grateful to Dr Luke Lavis for generously providing fluorophores, Satya Khuon and Dr Teng-Leong Chew at the Advanced Imaging Center (AIC), and our JHU colleagues Bram Lambrus, Tyler Moyer, Dr Alex Paix, Dr Jeremy Nathans, Rosanna Baker, and Gautam Prabhu, and Drs Cheryl Weaver and John Gibas (Olympus) for help and advice.

Funding: This work was supported, in part, by NIH grant R01AI066025 and an Innovator Award from Johns Hopkins University (both to SU). HHMI and the Packard Foundation funded our EPR spectrometer, DSC calorimeter, LB trough, and single-molecule TIRF microscope purchases. Much of the live-cell imaging data was collected at the AIC, which is supported by the Moore Foundation and HHMI's Janelia Research Campus. SU is also grateful to the Visiting Scientist program of Janelia Research Campus.

REFERENCES AND NOTES

1. Urban S, Snapshot: Cartography of Intramembrane Proteolysis. Cell 167, 1898–1898 e1891 (2016). [PubMed: 27984738]
2. Kinch LN, Grishin NV, Bioinformatics perspective on rhomboid intramembrane protease evolution and function. Biochim. Biophys. Acta 1828, 2937–2943 (2013). [PubMed: 23845876]
3. Shilo BZ, Developmental roles of Rhomboid proteases. Semin. Cell Dev. Biol 60, 5–9 (2016). [PubMed: 27423914]
4. Lastun VL, Grieve AG, Freeman M, Substrates and physiological functions of secretase rhomboid proteases. Semin. Cell Dev. Biol 60, 10–18 (2016). [PubMed: 27497690]
5. Spinazzi M, De Strooper B, PARL: The mitochondrial rhomboid protease. Semin. Cell Dev. Biol 60, 19–28 (2016). [PubMed: 27502471]
6. Dogga SK, Soldati-Favre D, Biology of rhomboid proteases in infectious diseases. Semin. Cell Dev. Biol 60, 38–45 (2016). [PubMed: 27567708]
7. Riestra AM et al., A Trichomonas vaginalis Rhomboid Protease and Its Substrate Modulate Parasite Attachment and Cytolysis of Host Cells. PLoS pathogens 11, e105294 (2015).
8. Sanders CR, Hutchison JM, Membrane properties that shape the evolution of membrane enzymes. Curr. Opin. Struct. Biol 51, 80–91 (2018). [PubMed: 29597094]
9. Dickey SW, Baker RP, Cho S, Urban S, Proteolysis inside the Membrane Is a Rate-Governed Reaction Not Driven by Substrate Affinity. Cell 155, 1270–1281 (2013). [PubMed: 24315097]
10. Kamp F et al., Intramembrane Proteolysis of beta-Amyloid Precursor Protein by gamma-Secretase Is an Unusually Slow Process. Biophys. J 108, 1229–1237 (2015). [PubMed: 25762334]
11. Bolduc DM, Montagna DR, Gu Y, Selkoe DJ, Wolfe MS, Nicastrin functions to sterically hinder gamma-secretase-substrate interactions driven by substrate transmembrane domain. Proc. Natl. Acad. Sci. U. S. A 113, E509–518 (2016). [PubMed: 26699478]
12. Szaruga M et al., Alzheimer's-Causing Mutations Shift Abeta Length by Destabilizing gamma-Secretase-Abetan Interactions. Cell 170, 443–456 e414 (2017). [PubMed: 28753424]
13. Young ME, Bell RL, Carroad PA, Estimation of diffusion coefficients of proteins. Biotechnol. Bioeng 22, 947–955 (1980).
14. Grimm JB et al., A general method to improve fluorophores for live-cell and single-molecule microscopy. Nat Methods 12, 244–250, 243 p following 250 (2015). [PubMed: 25599551]
15. Kreutzberger AJB, Urban S, Single-Molecule Analyses Reveal Rhomboid Proteins Are Strict and Functional Monomers in the Membrane. Biophys. J 115, 1755–1761 (2018). [PubMed: 30342748]
16. Saxton MJ, Jacobson K, Single-particle tracking: applications to membrane dynamics. Annu. Rev. Biophys. Biomol. Struct 26, 373–399 (1997). [PubMed: 9241424]
17. Abu-Arish A et al., Cholesterol modulates CFTR confinement in the plasma membrane of primary epithelial cells. Biophys. J 109, 85–94 (2015). [PubMed: 26153705]
18. Klein DC et al., CD14, TLR4 and TRAM Show Different Trafficking Dynamics During LPS Stimulation. Traffic (Copenhagen, Denmark) 16, 677–690 (2015).
19. Ma X et al., Lateral diffusion of TGF-beta type I receptor studied by single-molecule imaging. Biochem. Biophys. Res. Commun 356, 67–71 (2007). [PubMed: 17346672]
20. Marchetti L et al., Ligand signature in the membrane dynamics of single TrkA receptor molecules. J. Cell Sci 126, 4445–4456 (2013). [PubMed: 23886941]
21. O'Connell KM, Rolig AS, Whitesell JD, Tamkun MM, Kv2.1 potassium channels are retained within dynamic cell surface microdomains that are defined by a perimeter fence. J. Neurosci 26, 9609–9618 (2006). [PubMed: 16988031]
22. Schutz GJ et al., 3D Imaging of Individual Ion Channels in Live Cells at 40 nm Resolution. Single Molecules 1,25–31 (2000).
23. Xiao Z et al., Single-molecule study of lateral mobility of epidermal growth factor receptor 2/HER2 on activation. The journal of physical chemistry. B 112, 4140–4145 (2008). [PubMed: 18324805]

24. Yamamura H, Ikeda C, Suzuki Y, Ohya S, Imaizumi Y, Molecular assembly and dynamics of fluorescent protein-tagged single KCa1.1 channel in expression system and vascular smooth muscle cells. Am J Physiol Cell Physiol 302, C1257–1268 (2012). [PubMed: 22301058]
25. Poo M, Cone RA, Lateral diffusion of rhodopsin in the photoreceptor membrane. Nature 247, 438–441 (1974). [PubMed: 4818543]
26. Govardovskii VI, Korenyak DA, Shukolyukov SA, Zueva LV, Lateral diffusion of rhodopsin in photoreceptor membrane: a reappraisal. Mol. Vis 15, 1717–1729 (2009). [PubMed: 19727341]
27. Calvert PD et al., Membrane protein diffusion sets the speed of rod phototransduction. Nature 411, 90–94 (2001). [PubMed: 11333983]
28. Saffman PG, Delbruck M, Brownian motion in biological membranes. Proc. Natl. Acad. Sci. U. S. A 72, 3111–3113 (1975). [PubMed: 1059096]
29. Bondar AN, del Val C, White SH, Rhomboid protease dynamics and lipid interactions. Structure 17, 395–405 (2009). [PubMed: 19278654]
30. Ramadurai S, Duurkens R, Krasnikov VV, Poolman B, Lateral diffusion of membrane proteins: consequences of hydrophobic mismatch and lipid composition. Biophys. J 99, 1482–1489 (2010). [PubMed: 20816060]
31. Baker RP, Urban S, Cytosolic extensions directly regulate a rhomboid protease by modulating substrate gating. Nature 523, 101–105 (2015). [PubMed: 25970241]
32. Altenbach C, Greenhalgh DA, Khorana HG, Hubbell WL, A collision gradient method to determine the immersion depth of nitroxides in lipid bilayers: application to spin-labeled mutants of bacteriorhodopsin. Proc. Natl. Acad. Sci. U. S. A 91, 1667–1671 (1994). [PubMed: 8127863]
33. Baxt LA, Baker RP, Singh U, Urban S, An Entamoeba histolytica rhomboid protease with atypical specificity cleaves a surface lectin involved in phagocytosis and immune evasion. Genes Dev 22, 1636–1646 (2008). [PubMed: 18559479]
34. Rawlings ND et al., The MEROPS database of proteolytic enzymes, their substrates and inhibitors in 2017 and a comparison with peptidases in the PANTHER database. Nucleic Acids Res 46, D624–D632 (2018). [PubMed: 29145643]
35. Freeman M, The rhomboid-like superfamily: molecular mechanisms and biological roles. Annu. Rev. Cell Dev. Biol 30, 235–254 (2014). [PubMed: 25062361]
36. Cybulski LE, de Mendoza D, Bilayer hydrophobic thickness and integral membrane protein function. Current protein & peptide science 12, 760–766 (2011). [PubMed: 22044142]
37. Paix A et al., Precision genome editing using synthesis-dependent repair of Cas9-induced DNA breaks. Proc. Natl. Acad. Sci. U. S. A 114, E10745–E10754 (2017). [PubMed: 29183983]
38. Moyer TC, Holland AJ, Generation of a conditional analog-sensitive kinase in human cells using CRISPR/Cas9-mediated genome engineering. Methods Cell Biol 129, 19–36 (2015). [PubMed: 26175431]
39. Revyakin A et al., Transcription initiation by human RNA polymerase II visualized at single-molecule resolution. Genes Dev 26, 1691–1702 (2012). [PubMed: 22810624]
40. Chenouard N et al., Objective comparison of particle tracking methods. Nat Methods 11, 281–289 (2014). [PubMed: 24441936]
41. Sbalzarini IF, Koumoutsakos P, Feature point tracking and trajectory analysis for video imaging in cell biology. J. Struct. Biol 151, 182–195 (2005). [PubMed: 16043363]
42. Kalb E, Frey S, Tamm LK, Formation of supported planar bilayers by fusion of vesicles to supported phospholipid monolayers. Biochim. Biophys. Acta 1103, 307–316 (1992). [PubMed: 1311950]
43. Baker RP, Urban S, An Inducible Reconstitution System for the Real-Time Kinetic Analysis of Protease Activity and Inhibition Inside the Membrane. Methods Enzymol 584, 229–253 (2017). [PubMed: 28065265]
44. Budil DE, Lee S, Saxena S, Freed JH, Nonlinear-Least-Squares Analysis of Slow-Motion EPR Spectra in One and Two Dimensions Using a Modified Levenberg-Marquardt Algorithm. J. Magn. Reson 120, 155–189 (1996).
45. Osterberg JR et al., Membrane Docking of the Synaptotagmin 7 C2A Domain: Electron Paramagnetic Resonance Measurements Show Contributions from Two Membrane Binding Loops. Biochemistry (Mosc). 54, 5684–5695 (2015).

46. Oh KJ et al., Organization of diphtheria toxin T domain in bilayers: a site-directed spin labeling study. Science 273, 810–812 (1996). [PubMed: 8670424]
47. Almarza G, Sanchez F, Barrantes FJ, Transient cholesterol effects on nicotinic acetylcholine receptor cell-surface mobility. PloS one 9, e100346 (2014). [PubMed: 24971757]
48. Bates IR et al., Membrane lateral diffusion and capture of CFTR within transient confinement zones. Biophys. J 91, 1046–1058 (2006). [PubMed: 16714353]
49. Capps GG, Pine S, Edidin M, Zuniga MC, Short class I major histocompatibility complex cytoplasmic tails differing in charge detect arbiters of lateral diffusion in the plasma membrane. Biophys. J 86, 2896–2909 (2004). [PubMed: 15111406]
50. Xiao Z, Zhang W, Yang Y, Xu L, Fang X, Single-molecule diffusion study of activated EGFR implicates its endocytic pathway. Biochem. Biophys. Res. Commun 369, 730–734 (2008). [PubMed: 18313398]
51. Mirchev R, Lam A, Golan DE, Membrane compartmentalization in Southeast Asian ovalocytosis red blood cells. Br. J. Haematol 155, 111–121 (2011). [PubMed: 21793815]
52. Calebiro D et al., Single-molecule analysis of fluorescently labeled G-protein-coupled receptors reveals complexes with distinct dynamics and organization. Proc. Natl. Acad. Sci. U. S. A 110, 743–748 (2013). [PubMed: 23267088]
53. Crane JM, Verkman AS, Long-range nonanomalous diffusion of quantum dot-labeled aquaporin-1 water channels in the cell plasma membrane. Biophys. J 94, 702–713 (2008). [PubMed: 17890385]
54. Mainali D, Syed A, Arora N, Smith EA, Role of insulin receptor and insulin signaling on alphaPS2CbetaPS integrins' lateral diffusion. Eur. Biophys. J 43, 603–611 (2014). [PubMed: 25331198]
55. Mascalchi P, Lamort AS, Salome L, Dumas F, Single Particle Tracking reveals two distinct environments for CD4 receptors at the surface of living T lymphocytes. Biochem. Biophys. Res. Commun 417, 409–413 (2012). [PubMed: 22166195]
56. Notelaers K et al., Analysis of alpha3 GlyR single particle tracking in the cell membrane. Biochim. Biophys. Acta 1843, 544–553 (2014). [PubMed: 24316136]
57. Nechyporuk-Zloy V, Dieterich P, Oberleithner H, Stock C, Schwab A, Dynamics of single potassium channel proteins in the plasma membrane of migrating cells. Am J Physiol Cell Physiol 294, C1096–1102 (2008). [PubMed: 18287336]
58. Heidbreder M et al., TNF-alpha influences the lateral dynamics of TNF receptor I in living cells. Biochim. Biophys. Acta 1823, 1984–1989 (2012). [PubMed: 22749881]
59. Harms GS et al., Single-molecule imaging of l-type Ca(2+) channels in live cells. Biophys. J 81,2639–2646 (2001). [PubMed: 11606277]
60. Milenkovic L et al., Single-molecule imaging of Hedgehog pathway protein Smoothened in primary cilia reveals binding events regulated by Patched1. Proc. Natl. Acad. Sci. U. S. A 112, 8320–8325 (2015). [PubMed: 26100903]

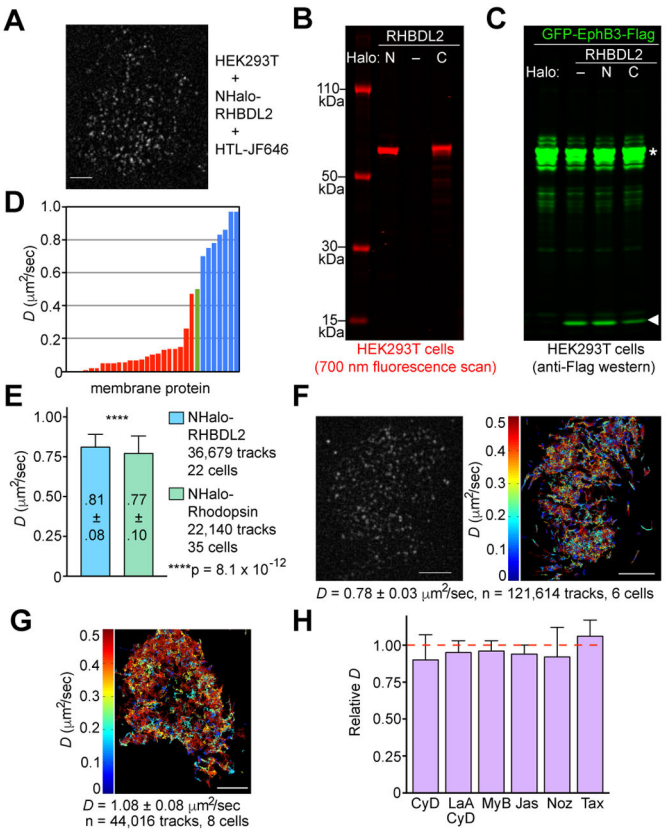

Figure 1. Single-molecule analysis of rhomboid protease and substrate diffusion in living human cells.

(**A**) smTIRF image of a HEK293T cell expressing Halo-RHBDL2 labeled with HTL-JF646. White scale bars indicate 5 μm throughout. (**B**) Electrophoretic analysis of whole cell lysates of HTL-JF646-labeled HEK293T cells expressing the indicated RHBDL2 construct. (**C**) Processing of GFP-Ephrin B3-Flag in transfected HEK293T cells co-expressing Halo-tagged versus untagged RHBDL2. Denoted are uncut (asterisks) and cut (arrow) fragments. (**D**) *D* of >20 membrane proteins measured by single-particle tracking (red bars), classical rhodopsin studies (green bar), and rhomboid proteins (blue bars). See Table S1 for protein names/sources.(**E**) Parallel comparison of Halo-RHBDL2 versus Halo-Rhodopsin diffusion in HEK293T cells.(**F**) smTIRF image of a HEK293T cell with its endogenous RHBDL2 tagged with Halo (labeled with HTL-JF549), and single-molecule tracks of the same cell over 2,000 frames. Tracks are color-coded by *D*, and the mean±s.d. is shown for the indicated number of cells throughout. (**G**) Tracks of JF549-SNAP-Ephrin B3-Flag diffusion in HEK293T cells. (**H**) Halo-RHBDL2 mobility in living HEK293T cells treated with actin or microtubule destabilizing or stabilizing agents (see Methods). Means are normalized to each untreated sample analysed in parallel. Cohen's d-values ranged from 0.004-0.21, indicating effect sizes between very small and small.

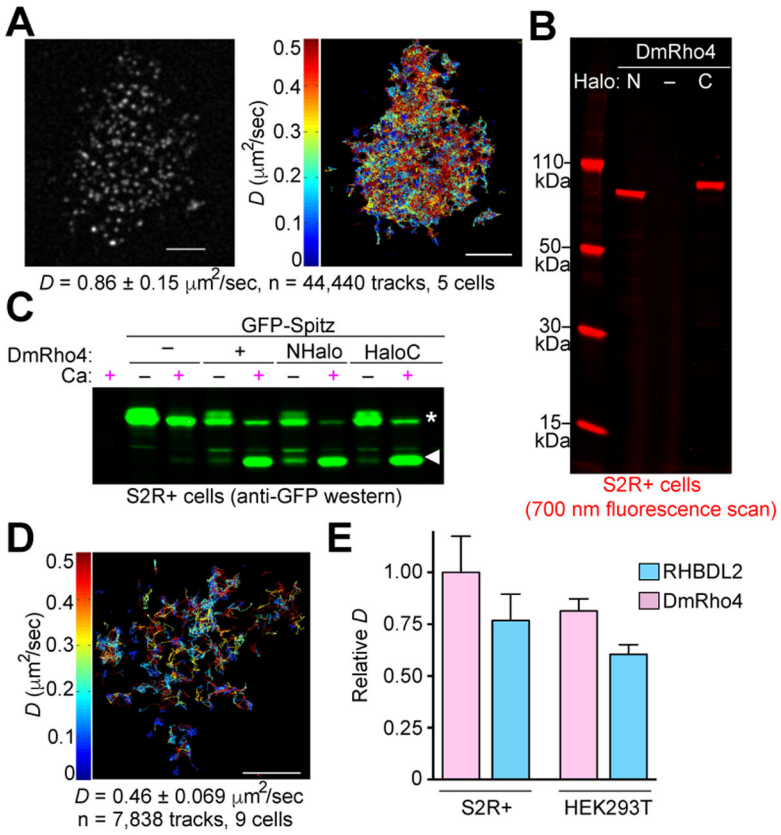

Figure 2. Single-molecule analysis of rhomboid protease and substrate diffusion in living *Drosophila* cells.

(**A**) smTIRF image of DmRho4-HaloC-JF549 molecules in a S2R+ cell (left), and their diffusion tracks (right, recorded for 2,000 frames at 25 Hz). Tracks are color-coded by *D*, the mean±s.d. is shown for the indicated number of cells, and white scale bars indicate 5 μm throughout. (**B**) Electrophoretic analysis of whole cell lysates of HTL-JF646-labeled S2R+ cells expressing the indicated DmRho4 construct. (**C**) Processing of GFP-Spitz in transfected S2R+ cells co-expressing Halo-tagged versus untagged DmRho4, and in the absence (−) or presence (+) of Ca^{2+} stimulation. Uncut (asterisks) and cut (arrow) fragments are indicated. Untransfected cells were analysed in the leftmost lane. (**D**) Tracks of JF549-SNAP-Spitz diffusing in a S2R+ cell. (**E**) *D* comparisons: DmRho4 diffused faster than RHBDL2 in both S2R+ cells ($p=2.0\times10^{-184}$) and HEK293T cells ($p=4.1\times10^{-244}$), and diffusion of both proteins was faster in S2R+ cells than in HEK293T cells (DmR4, $p=1.6\times10^{-195}$; RHBDL2, $p=3.4\times10^{-233}$). Data is normalized to DmRho4 in S2R+ cells

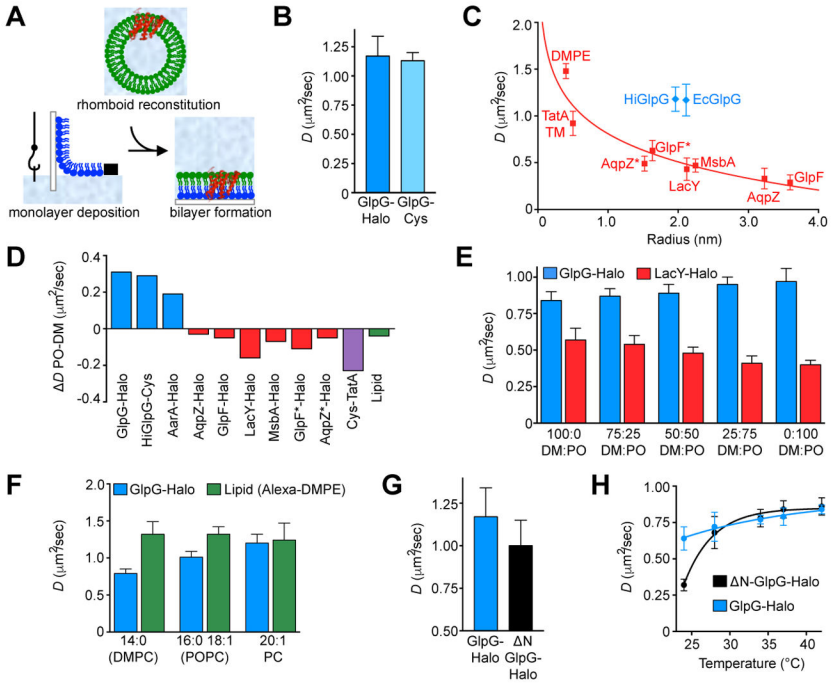

Figure 3. Rhomboid diffuses above the viscosity limit in planar supported lipid bilayers.

(**A**) Three-step method for nanofabricating planar supported lipid bilayers for visualizing rhomboid protein diffusion. (**B**) *D* of GlpG-Halo and GlpG-Cys in 70:30 POPE:POPG and at 37°C (p=0.0098, d=0.08). (**C**) Saffman-Delbrück relation plotting *D* of Halo-tagged or Cystagged proteins, a synthetic transmembrane peptide from TatA (9), and a lipid (Alexa647-DMPE) in planar supported bilayers composed of 70:30 POPE:POPG and at 37°C against their molecular radii. Asterisks indicate monomer mutants. (**D**) Difference of *D* in 70:30 POPE:POPG (natural thickness) minus *D* in 70:30 DMPE:DMPG (thin) at 37°C. (**E**) *D* of GlpG-Halo versus LacY-Halo in different mole fractions of DMPC versus POPC. (**F**) *D* of Halo-tagged GlpG and a lipid in planar supported bilayers of different thickness and at 37°C (DMPC p=1.1 × 10^{-83}, POPC p=5.2 × 10^{-21}, 20:1 PC p=0.13). (**G**) *D* of GlpG-Halo and ΔN-GlpG-Halo in planar supported bilayers composed of 70:30 POPE:POPG at 37°C (p=0.0018, d=0.22). (**H**) *D* of GlpG-Halo and ΔN-GlpG-Halo in planar supported bilayers composed of DMPC and at five different temperatures. Only diffusion by full-length GlpG remained linear near the DMPC transition temperature.

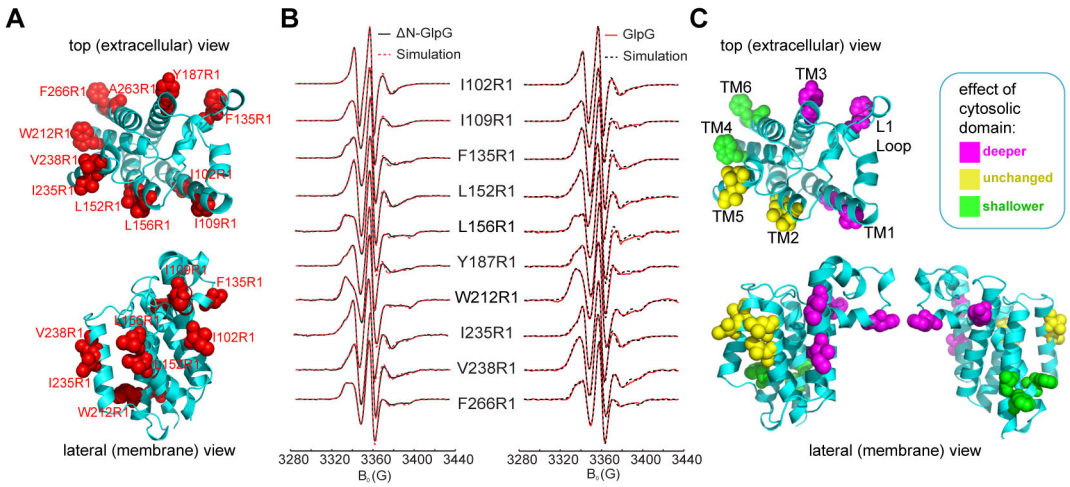

Figure 4. Membrane position of *E. coli* GlpG assessed by EPR spectroscopy.

(**A**) Positions of 11 membrane-facing residues (in red spheres) on GlpG and ΔN-GlpG that were used for nitroxide spin labeling. (**B**) Continuous-wave EPR spectra of GlpG (red lines) and ΔN-GlpG (black lines) harbouring a single nitroxide probe at the indicated positions. Proteins were reconstituted into proteoliposomes comprised of *E. coli* lipids, spectra were recorded at 298°K, and deconvoluted by MOMD spectral simulation (dashed lines). (**C**) Membrane-immersion depths changed when GlpG contained its cytosolic domain; residue positions in red adopted deeper membrane immersion while residue positions in green adopted more shallow positions in the membrane when the cytosolic domain was present. Residue positions in yellow remained unchanged. See Tables S2 and S3 for spin probe accessibility parameters and immersion depth calculations.

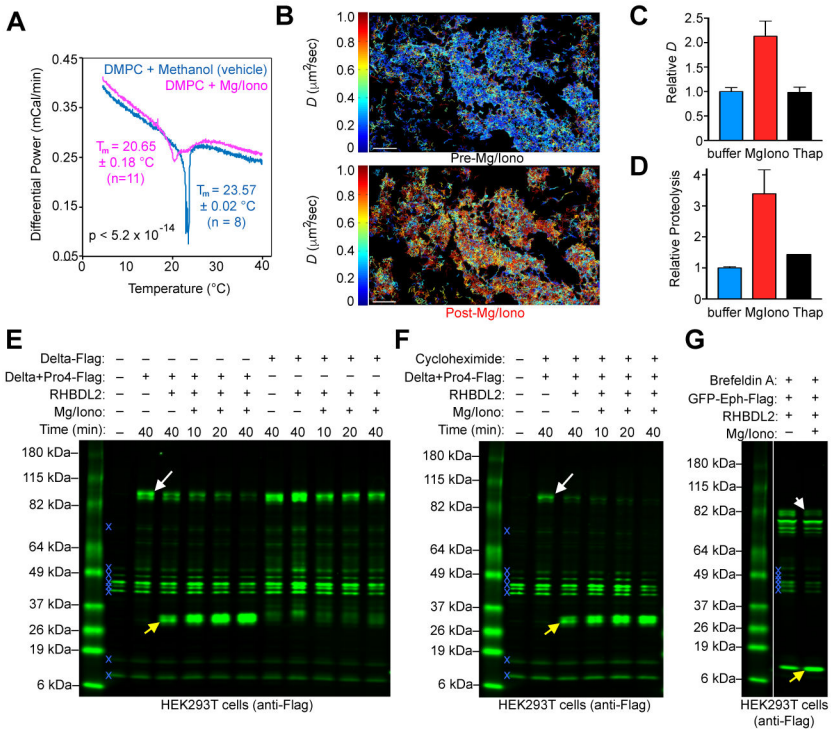

Figure 5. Rhomboid proteolysis is diffusion-limited in living cells.

(**A**) Calorigrams of DMPC vesicles showing a shift in transition temperature (T_m) and trough broadening exerted by Mg^{2+}/Ionomycin relative to methanol vehicle. (**B**) NHalo-RHBDL2 molecule tracks (colored by *D*) on the same field of HEK293T cells before and after Mg^{2+}/Ionomycin addition. White scale bars indicate 5 μm. (**C**) Diffusion of NHalo-RHBDL2 in living HEK293T cells treated with Mg^{2+}/Ionomycin (MgIono) or Thapsigargin (Thap) versus buffer (normalized to the untreated mean). Mglono accelerated diffusion ($p<10^{-323}$, Cohen's h=0.83, large effect). (**D**) Protease activity of NHalo-RHBDL2 in HEK293T cells treated with Mglono or Thap relative to buffer. (**E**) Increasing diffusion did not induce proteolysis of the non-substrate Delta, but dramatically and rapidly (within 10 minutes) increased RHBDL2-catalyzed proteolysis of an engineered form of Delta carrying a single proline in its transmembrane segment (Delta+Pro4). Denoted throughout are the full-length protein (white arrow), the cleaved form (yellow arrow), and immunoreactive background bands in untransfected cells (blue x) that served as loading controls. (**F**) Blocking protein synthesis with 100 μg/mL cycloheximide did not affect Mg^{2+}/Ionomycin-stimulated processing of Delta+Pro4 by RHBDL2. (**G**) Blocking subcellular trafficking with 2.8 μg/mL Brefeldin A did not affect Mg^{2+}/Ionomycin-stimulated processing of Ephrin by RHBDL2. Note conversion of the glycosylated, full-length cell surface population (white arrow) into the cleaved form (yellow arrow).

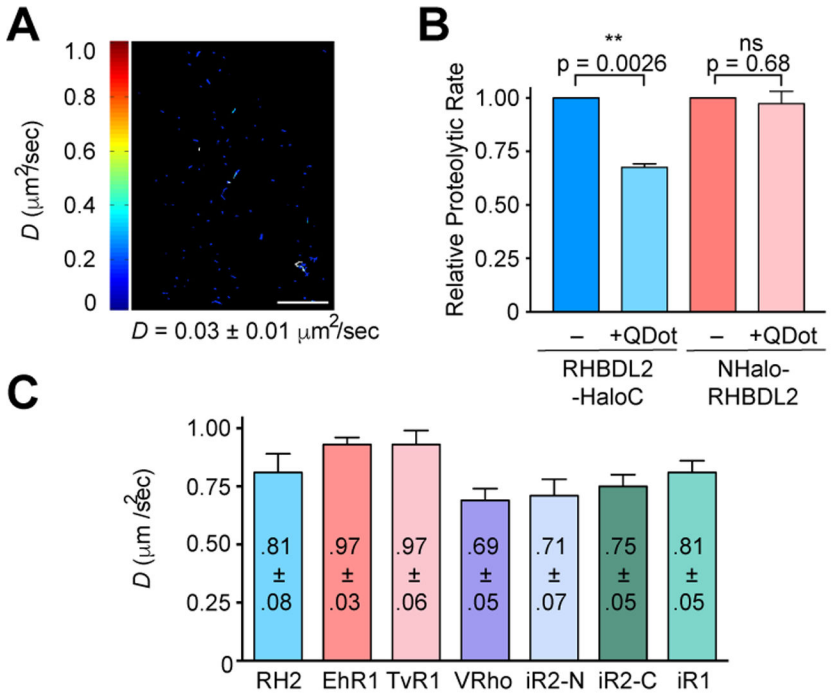

Figure 6. Experimental and evolutionary tuning of rhomboid diffusivity.

(**A**) Tracks (colored by *D*) of RHBDL2-HaloC molecule diffusion in HEK293T cell after being complexed with quantum dots. Mean±s.d. is shown. White scale bar indicates 5 μm. (**B**) Relative protease activity of RHBDL2-HaloC (extracellular tag) versus NHalo-RHBDL2 (cytoplasmic tag) on Ephrin B3 in HEK293T cells treated with extracellular quantum dots relative to buffer. (**C**) *D* of NHalo-RHBDL2 (RH2), EhROM1-HaloC (EhR1), NHalo-TvROM1 (TvR1), RHBDL3/Ventrhoid-HaloC (VRho), NHalo-iRhom2 (N-iR2), iRhom2-HaloC (iR2-C), and iRhom1-HaloC (iR1) in living HEK293T cells. Mean±s.d. of >18,000 tracks (at 64Hz) from ≥5 cells is shown.

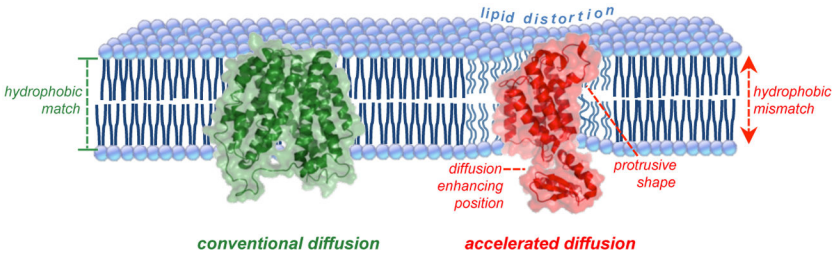

Figure 7. Boosting protein diffusion through the membrane.

Rhomboid's irregular shape, repositioning in the membrane by the cytosolic domain, and hydrophobic mismatch synergize to boost its diffusion beyond the viscosity limit of the membrane by distorting surrounding lipids (depicted as curved tails on right). Other membrane proteins (in green, left) that lack these disruptive features fit more regularly into the membrane and experience conventional diffusion.